ACS APPLIED MATERIALS & INTERFACES

Research Article

Cite This: ACS Appl. Mater. Interfaces 2019, 11, 47340−47349

www.acsami.org

A Hydrophobic, Self-Powered, Electromagnetic Shielding PVDF-Based Wearable Device for Human Body Monitoring and Protection

Min Sang,[†] Sheng Wang,[‡] Shuai Liu,[‡] Mei Liu,[†] Linfeng Bai,[†] Wanquan Jiang,*[,†] Shouhu Xuan,*[,‡] and Xinglong Gong*[,‡]

[†]Department of Chemistry, University of Science and Technology of China, Hefei, Anhui 230026, PR China

[‡]CAS Key Laboratory of Mechanical Behavior and Design of Materials, Department of Modern Mechanics, CAS Center for Excellence in Complex System Mechanics, University of Science and Technology of China, Hefei, Anhui 230027, PR China

Supporting Information

ABSTRACT: With the rapid development of the electronics, information technology, and wearable devices, problems of the power crisis and electromagnetic radiation pollution have emerged. A piezoelectric wearable textile combined with electromagnetic shielding performance has become a favorable solution. Herein, a multifunctional PVDF-based wearable sensor with both electromagnetic shielding function and human body monitoring performance is proposed by incorporating silver nanowires (Ag NWs) and multiwall carbon nanotubes (MWCNTs) hybrid-networks into PVDF-casted commercial nonwoven fabrics (NWF). The coordination of Ag NWs and MWCNTs networks ensures the ideal electrical conductivity and mechanical strength. The maximum shielding value of the developed sensor reaches up to 34 dB when the area densities of the Ag NWs and MWCNT are kept at 1.9 and 2.0 mg/cm^2, respectively. Additionally, the hydrophobicity of the as-proposed sensor (water contact angle of ∼110.0°) ensures the self-cleaning function and makes it resistive against water and dirt. Moreover, the sensor possesses a force-sensing property by generating different piezoelectric voltages (0, 0.4, 1.0, and 1.5 V) when stimulated by various forces (0, 20, 44, and 60 N). Not only can it respond to different external stress in a timely manner (response sensitivity of ∼0.024 V/N, response time of ∼35 ms), but it can also monitor different body movements, such as joint bending, running, and jumping. This work opens up a new prospect of monitoring the human body as well as protecting human health from electromagnetic radiation surroundings.

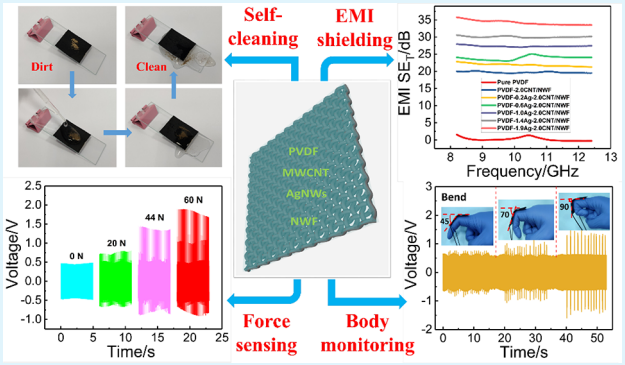

KEYWORDS: *conductive networks, piezoelectric PVDF polymer, electromagnetic interference (EMI) shielding, sensing, human body monitoring*

1. INTRODUCTION

With the popularization of smart electronics and wearable devices, electromagnetic radiation pollution has become a severe problem because it often causes harmful effects on human beings. To solve this issue effectively, high-performance electromagnetic shielding materials have attracted increasing interests, and many important studies have been performed.[1−7] According to electromagnetic theories,[8,9] the shielding attenuation of the electromagnetic wave was usually achieved through the interface reflection and internal absorption. Generally, materials which possessed higher electrical conductivity would exhibit higher reflection and loss ability and thus had better shielding performance. During the past decade, many conductive materials, such as MXene,[10,11] metallic nanowires,[12] carbon nanotubes,[13] and graphene[14] have been applied in the field of electromagnetic shielding. Among them, silver nanowires (Ag NWs)[15,16] and multiwall carbon nanotubes (MWCNTs)[17,18] have been considered to be promising conductive fillers to assemble electromagnetic interference (EMI) shielding composite structures because of their excellent electrical conductivity, controllable aspect ratio, and favorable mechanical flexibility.

Recently, flexible wearable pressure sensors have gained tremendous interests for unique sensing applications in human body monitoring, electronic skin, and artificial intelligence.[19−22] They could mimic human skin by transducing external stimuli such as pressure, strain, and temperature into an electrical signal. Usually, the aforementioned functions could be achieved by flexible wearable pressure sensors that exploit various sensing mechanisms, including piezoresistive,[23,24] piezocapacitive,[25,26] piezoelectric,[27,28] and triboelectric[29,30] effects. Typically, piezoelectric sensors are attractive because of their self-powered sensing behavior; thus, much attention has been paid to develop flexible pressure

Received: September 6, 2019
Accepted: November 19, 2019
Published: November 19, 2019

DOI: 10.1021/acsami.9b16120
ACS Appl. Mater. Interfaces 2019, 11, 47340−47349

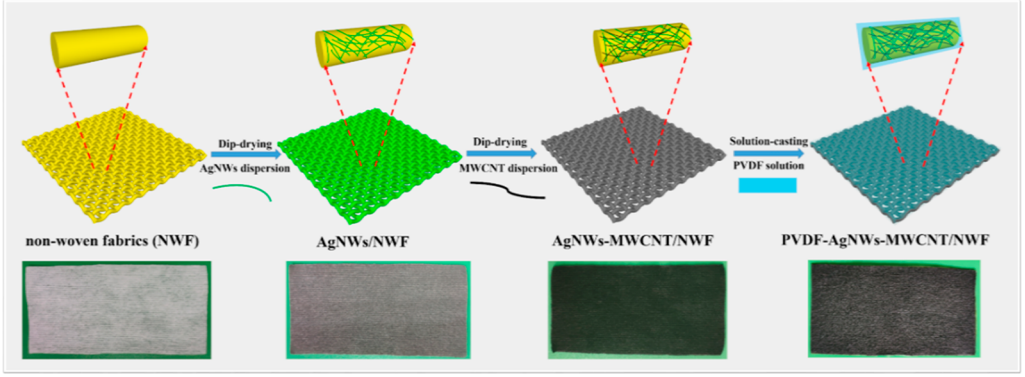

Figure 1. Schematic illustration of fabrication steps of the as-prepared PVDF-Ag-CNT/NWF composite.

sensors with piezoelectric materials. In comparison to the traditional inorganic piezoelectric materials like ZnO and barium titanate (BTO), organic ferroelectric polymer poly(vinylidene fluoride) (PVDF)[31−38] is preferred because of desirable flexibility, excellent stability, low density, and low-cost processing, and it has a very broad application prospect in the fields of sensing and human body monitoring.

In consideration of the increasing electromagnetic radiation in our current daily life and future aerospace technology, developing wearable devices with electromagnetic shielding characteristic is desirable to reduce the biological damage effect. In this case, the flexible wearable pressure sensor with electromagnetic shielding performance shows great competitiveness because it can protect human beings from electromagnetic radiation while exhibiting its sensing ability. Zhang and co-workers[39] reported a stretchable electromagnetic shielding hybrid nanogenerator (ES-HNG) which could not only protect and monitor human health but also scavenge thermal and mechanical energy from the living environment. Interestingly, the ES-HNG was able to monitor human health by attaching it on the human abdomen to be a self-powered sensor. Pu et al.[40] presented a multifunctional electronic skin with pressure-sensing and electromagnetic-shielding abilities. To demonstrate the utility of this electronic skin, they also fabricated a personalized intelligent glove made of these electronic skins. As a result, the multifunctional wearable device with a self-powered nature and electromagnetic shielding performance is becoming an important research challenge to overcome.

Herein, we developed a hydrophobic self-cleaning, flexible, and wearable PVDF-based sensor, which can not only monitor movements of the human body but also protect human beings from electromagnetic radiation. The multifunctional sensor is composed of nonwoven fabrics (NWF) with silver nanowires (Ag NWs), multiwall carbon nanotubes (MWCNTs) conductive networks, and PVDF piezoelectric polymers. These materials have the following advantages: (1) Ag NWs, as a kind of precious metal nanomaterial, possess very good conductivity, but they are expensive and easy to be oxidized; (2) MWCNTs, as a kind of one-dimensional conductive nanomaterial, are cheap and stable. Furthermore, MWCNTs exhibit excellent mechanical strength and toughness. The combination of Ag NWs and MWCNTs can not only endow the composite with high electrical conductivity but also strengthen the mechanical properties of the material. Therefore, it is expected to show good electromagnetic shielding performance and ideal mechanical properties. Moreover, because of the piezoelectricity of the PVDF polymer, the sensor can detect various pressure stimuli. Finally, different human-motion-related stresses induced by joint bending, running, and jumping were also discriminated. Because of the self-powered nature and electromagnetic shielding characteristic, this multifunctional PVDF-based composite possesses wide potential in health monitoring, energy harvesting, low power electronics, and EMI shielding, which also provides a powerful guide for the development of other multifunctional materials.

2. EXPERIMENTAL SECTION

2.1. Materials. Poly(vinylidene fluoride) (PVDF, MW ≈ 53000) pellets were purchased from Sigma-Aldrich, U.S.A. *N*-Methyl pyrrolidone (NMP, AR > 99.0%, GC) and polyvinylpyrrolidone (MW ≈ 40 000) were provided by Aladdin chemical Co., Ltd., China. The alcohol dispersion of MWCNTs (67 wt %, purity higher than 90%) with a diameter of 10−20 nm and a length of 10−30 μm was purchased from Chinese Academy of Sciences, Chengdu Organic Chemicals Co., Ltd., China. Silver nitrate ($AgNO_3$), glycerol ($C_3H_8O_3$), and sodium chloride (NaCl) were received from Sinopharm Chemical Reagent Co. Ltd., China. The nonwoven fabrics (NWF) and the conductive copper tape were commercially available products, China. All reagents were used without further purification, and distilled water was used.

2.2. Synthesis of Ag NWs' Solution. Briefly, 5.86 g of polyvinylpyrrolidone was completely dissolved into 190 mL of glycerol at 90 °C under stirring, and then the solution was cooled to 50 °C. Continuously, 1.58 g of $AgNO_3$ powder and a mixed solution containing 10 mL of glycerol, 59 mg of NaCl, and 0.5 mL of distilled water were poured into the flask under stirring and heating. Until the reaction temperature reached to 210 °C, the gray-green solution could be obtained. The resultant solution was placed into the beaker and cooled to 90 °C, and then 200 mL of distilled water was added. The mixture was allowed to sit undisturbed for 1 week to maintain stability; subsequently, it was centrifuged and washed with distilled water and ethanol each for three times. Finally, Ag NWs were suspended in ethanol to obtain the solution of Ag NWs.[41]

2.3. Fabrication of the PVDF-Based Wearable Sensor with Both Electromagnetic Shielding Performance and Human Body Monitoring. The PVDF-based wearable sensor was prepared via a facile dip-drying and solution-casting approach (Figure 1). Here, the PVDF stock solution was prepared by dissolving 10.6 g of PVDF pellets in 60 mL of NMP at 60 °C with magnetic stirring in the oil bath for 2 h for standby application. The density of NMP solvent is 1.028 g/cm^3; thus, the concentration of PVDF solution is calculated as 17 wt %. First, the NWF was impregnated in the dispersion of Ag NWs and then dried in the oven at 60 °C for 5 min after each impregnation. Subsequently, the obtained Ag NWs/NWF was further decorated with the alcohol dispersion of MWCNTs by the same dip-drying method. Finally, the PVDF stock solution was casted on the Ag NWs-MWCNT/NWF onto a clean and horizontal glass plate in a

DOI: 10.1021/acsami.9b16120
ACS Appl. Mater. Interfaces 2019, 11, 47340−47349

vacuum oven, evaporated at 80 °C for 12 h, and annealed at 120 °C for 8 h to obtain the PVDF-based composite. Here, the contents of Ag NWs and MWCNT were determined by controlling the impregnation numbers. The volume of the casted PVDF solution was identical for every sample (4 mL). At a fixed MWCNTs area density of 2.0 mg/cm^2, a series of AgNWs area density was determined as 0, 0.2, 0.6, 1.0, 1.4, and 1.9 mg/cm^2, and the corresponding samples were labeled as PVDF-2.0CNT/NWF, PVDF-0.2Ag-2.0CNT/NWF, PVDF-0.6Ag-2.0CNT/NWF, PVDF-1.0Ag-2.0CNT/NWF, PVDF-1.4Ag-2.0CNT/NWF, and PVDF-1.9Ag-2.0CNT/NWF, respectively. Besides, the pure PVDF film and the sample without impregnation of Ag NWs and MWCNTs' dispersion named as PVDF/NWF were also fabricated as references. By using a digimatic micrometer measurement (Sanliang Corporation, 0−25 mm), the final thicknesses of PVDF/NWF, PVDF-2.0CNT/NWF, PVDF-0.2Ag-2.0CNT/NWF, PVDF-0.6Ag-2.0CNT/NWF, PVDF- 1.0Ag-2.0CNT/NWF, PVDF-1.4Ag-2.0CNT/NWF, and PVDF-1.9Ag-2.0CNT/NWF were approximately 304, 332, 347, 359, 367, 377, and 390 μm, respectively. For the sensor fabrication, the commercially available conductive copper tape was used as the top and bottom electrode and was directly attached to the upper and lower surface of the PVDF-based composite. To prevent the charge leakage caused by making contact with the outside, a layer of black insulation tape was affixed to the electrode. By using the digimatic micrometer, the thicknesses of conductive copper electrode, black insulation tape, and PVDF-1.9Ag-2.0CNT/NWF composite were measured as 55, 120, and 390 μm, respectively; thus, the total thickness of the as-prepared PVDF-based device was 740 μm. Besides, the size of the PVDF-based device was 3 × 6 cm^2.

2.4. Characterization. The surface morphology and cross-sectional topography of the synthesized Ag NWs and PVDF-based sensor was characterized by scanning electron microscopy (GeminiSEM 500, ZEISS) and transmission electron microscopy (TEM, H-7650). The crystalline phases of the PVDF-based sensor were identified by X-ray diffraction (XRD) (SmartLab9 kW, Japan). The Fourier transform infrared spectroscopy (FTIR) was performed using a Bruker alpha apparatus in ATR mode from 4000 to 400 cm^{-1} using 24 scans at a resolution of 4 cm^{-1}. The ferroelecticity and inverse piezoelectricity of the PVDF-based composite were tested using the ferroelectric testing system (P-LC100). The tensile properties of the PVDF-based sensor were examined by the Material Test System (MTS). The effective size of the sample is 1 × 4 cm^2, and the tensile speed is set as 3 mm/min. The cyclic bending test for electromagnetic shielding performance was conducted by DMA equipment (TA ElectroForce 3220, TA Instruments, America). The electricity conductivity was measured by the standard four-point contact method on a four-point probe (FT-340, Ningbo rooko instrument Co., Ltd., China). The electromagnetic shielding performance of the samples was obtained by ASTM D 4935-89 using a vector network analyzer (AV3672, China electronics technology instruments Co., Ltd.) in the 8−12 GHz region (X-Band). Water contact angles were measured by the CAST 2.0 contact-angle-analysis system (Solon Information Technology) at ambient temperature with a water droplet of 3 μL in volume. The piezoelectric tests were conducted by an oscillator (JZK-10) (bought from Sinocera. Piezotronics, Inc., China) and corresponding output signals of the as-prepared PVDF-based sensor were recorded by a digital multimeter (DMM6001). The thickness of the PVDF-based composite was measured by a digimatic micrometer (Sanliang Corporation, 0−25 mm).

3. RESULTS AND DISCUSSION

3.1. Characterization of the As-Synthesized Ag NWs and PVDF-Based Composite. Figure 2 exhibits the morphological and structure characterization of as-prepared Ag NWs. From SEM and TEM images, the as-prepared Ag NWs show high purity, and rare silver nanoparticles can be observed (Figure 2a,b). Moreover, the synthesized Ag NWs are uniform in diameter of 59 nm and with length in the range of about 1−15 μm, which gives an aspect ratio of about 17−254

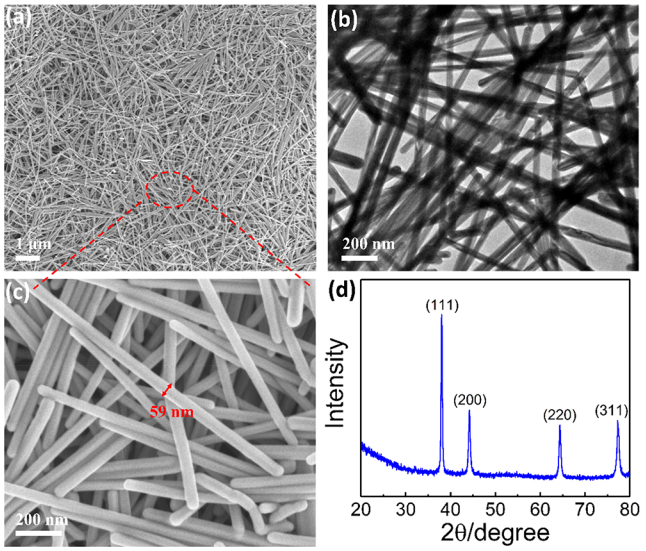

Figure 2. SEM images (a, c), TEM image (b), and XRD pattern (d) of Ag NWs.

(Figure 2a,c). These results are basically consistent with the literature report.[41] Besides, the crystal structure of Ag NWs was identified by the XRD patterns (Figure 2d). The four peaks were indexed as (111), (200), (220), and (311) facets of the Ag NWs, which demonstrated the effective synthesis of Ag NWs. Besides, the SEM and TEM images of the purchased MWCNTs' alcohol dispersion with a diameter of 10−20 nm and a length of 10−30 μm are shown in Figure S1. Thus, aspect ratio was calculated to be in the range of about 500−3000.

The PVDF-based wearable sensor was prepared via a facile dip-drying and solution-casting approach. During the preparation, the structure evolution was tracked by scanning electron microscopy (SEM, Figure 3). The pristine NWF was a kind of fabric with an irregular network structure formed by a random arrangement of bundles (Figure 3a). Without any modification, the surface of the long microfibers was smooth (Figure 3e,i). This network structure was favorable for the subsequent adhesion of Ag NWs and MWCNTs. Then, the NWF was immersed into the Ag NWs suspension for decorating Ag NWs. After it was dried, it was observed that the surface of the NWF was randomly covered by an interconnected Ag NWs network. Although the fiber surface of the NWF became a little rough, its originally irregular reticulated structure could be clearly observed (Figure 3b,f,j). Subsequently, the fiber surface of the NWF turns very rough after further coating the MWCNTs. The coating not only existed on the individual fiber surface but also filled the gap between fibers, so that the network structure of the NWF could no longer be clearly seen (Figure 3c,g,k). Here, the hybrid Ag NWs and MWCNTs coating on the NWF could form effective conductive paths, which was beneficial for improving the conductivity. To more clearly show the interface formation process between textile and nanomaterials, the high-magnification SEM images (Figure S2), elemental mapping images, and EDS spectrum (Figures S3−S6) of the nonwoven fabrics (NWF), 1.9Ag NWs/NWF, 2.0CNT/NWF, and 1.9Ag NWs-2.0CNT/NWF were also supplied (Supporting Information). Finally, PVDF polymer was casted on the surface of the Ag NWs-MWCNT/NWF hybrid network, the surface of the final product became smooth, and the NWF, Ag NWs, and MWCNTs were all

DOI: 10.1021/acsami.9b16120
ACS Appl. Mater. Interfaces 2019, 11, 47340−47349

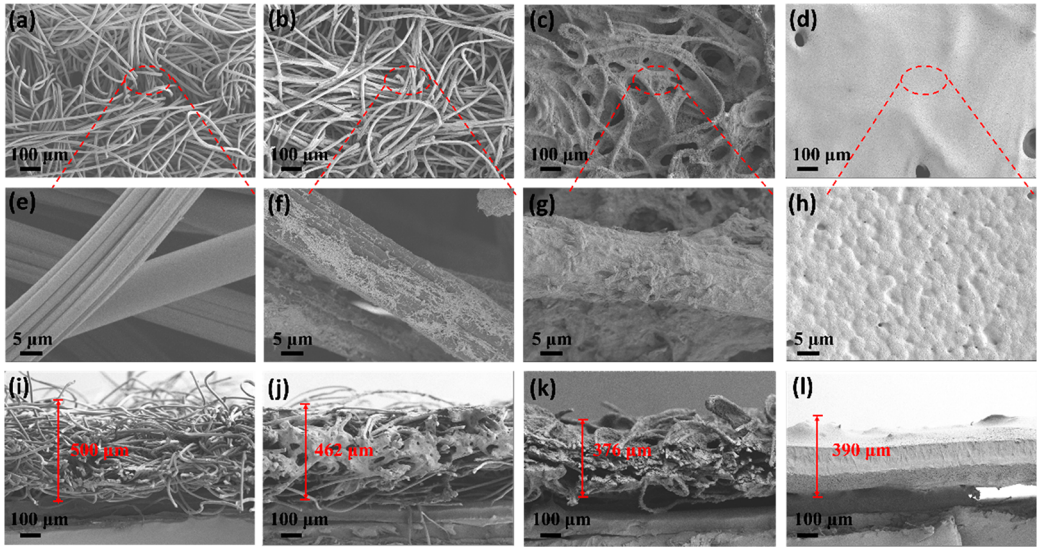

Figure 3. SEM images of the pristine NWF (a, e, i), Ag NWs/NWF with Ag NWs area density of 1.9 mg/cm^2 (b, f, j), Ag NWs-MWCNT/NWF with Ag NWs area density of 1.9 mg/cm^2 and MWCNT area density of 2.0 mg/cm^2 (c, g, k) and the PVDF-1.9Ag-2.0CNT/NWF (d, h, l).

covered by the PVDF polymer (Figure 3d,h,l). In addition, the cross-sectional morphology of the pristine nonwoven fabrics (NWF) shows a loose structure with the thickness of about 500 μm (Figure 3i). After Ag NWs were coated, it was seen that the morphology had slightly changed, and the cross-sectional structure became a little tighter (462 μm), indicating Ag NWs were successfully embedded into the interior of the NWF (Figure 3j). Figure 3k exhibits the cross-sectional image of Ag NWs/NWF modified by MWCNTs. Obviously, the cross-sectional structure was especially denser with the thickness of 376 μm. Because of the impregnation of Ag NWs and MWCNTs on the NWF, the loose cross-sectional structure of the original NWF cannot be observed, which reveals that MWCNTs and Ag NWs can be embedded in the interior of the NWF and makes the original fiber network structure of the NWF be denser. At last, PVDF-based composite with Ag NWs-MWCNT/NWF hybrid-networks encapsulated by PVDF matrix was obtained.

The FTIR and XRD measurements were used to investigate the crystalline phase of the as-prepared PVDF-based composite. As we know, PVDF is a typical piezoelectric polymer with five distinct crystalline phases α, β, γ, δ, and ε, among which the β-phase has the best piezoelectric performance, followed by γ-phase. As for the pure PVDF film, the peaks at 811, 833, and 1230 cm^{-1} prove the existence of γ-phase crystalline structure, and the peak of 769 cm^{-1} is attributed to the α-phase (Figure 4a).[42] After the PVDF solution was casted onto the NWF to form PVDF/NWF, the structure of the crystalline phase does not change. Similarly, the PVDF-2.0CNT/NWF and PVDF-1.9Ag-2.0CNT/NWF also show the piezoelectric γ-phase. Although the developed PVDF-based composite does not contain an obvious β-phase, it contains an obvious γ-phase which will also be expected for showing a piezoelectric effect.[43−46] Moreover, the γ-phase contents of pure PVDF, PVDF/NWF, PVDF-2.0CNT/NWF, and PVDF-1.9Ag-2.0CNT/NWF composite are calculated as 93%, 88%, 92%, and 90%, respectively, revealing that the PVDF-based composite has a high γ-phase content (Figure S7). The XRD pattern of the final products is shown in Figure 4d. It is clear from the XRD pattern that the peak at 20.2° corresponds to the β-phase crystalline structure, and the peak

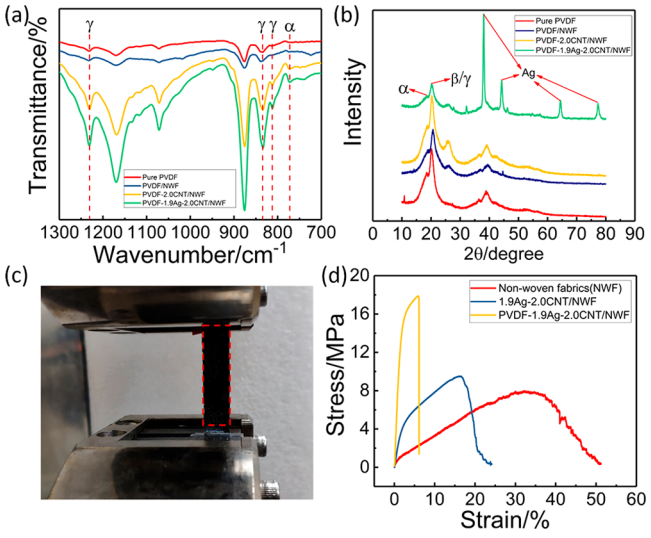

Figure 4. FTIR spectrum (a) and XRD pattern (b) of pure PVDF film, PVDF/NWF, PVDF-2.0CNT/NWF, and PVDF-1.9Ag-2.0CNT/NWF. Experimental device of uniaxial tensile measurement using MTS (c). The tensile stress−strain curves of NWF, 1.9Ag-2.0CNT/NWF, and PVDF-1.9Ag-2.0CNT/NWF (d).

at 18.4°corresponds to the α-phase, in which the overall display is a typical γ-phase peak.[47] These results are in excellent agreement with the FTIR test results. Besides, the ferroelectricity and inverse piezoelectricity of PVDF-1.9Ag-2.0CNT/NWF composite were also shown by polarization−electric field (P−E) hysteresis loops and electric field induced strain curves (butterfly loops) (Figure S8). As for PVDF-1.9Ag-2.0CNT/NWF composite, it is worth mentioning that the peaks observed at 38°, 44°, 64°, and 77° (Figure 4b) are corresponding to the crystalline structure of Ag, which also testifies the successful loading of Ag NWs onto the NWF.

To characterize the mechanical property of the as-prepared PVDF-based composite, tensile tests using MTS system were carried out (Figure 4c). Figure 4d displays the representative tensile stress−strain curves, which shows conspicuous yielding and strain hardening of the as-fabricated PVDF-based

DOI: 10.1021/acsami.9b16120
ACS Appl. Mater. Interfaces 2019, 11, 47340−47349

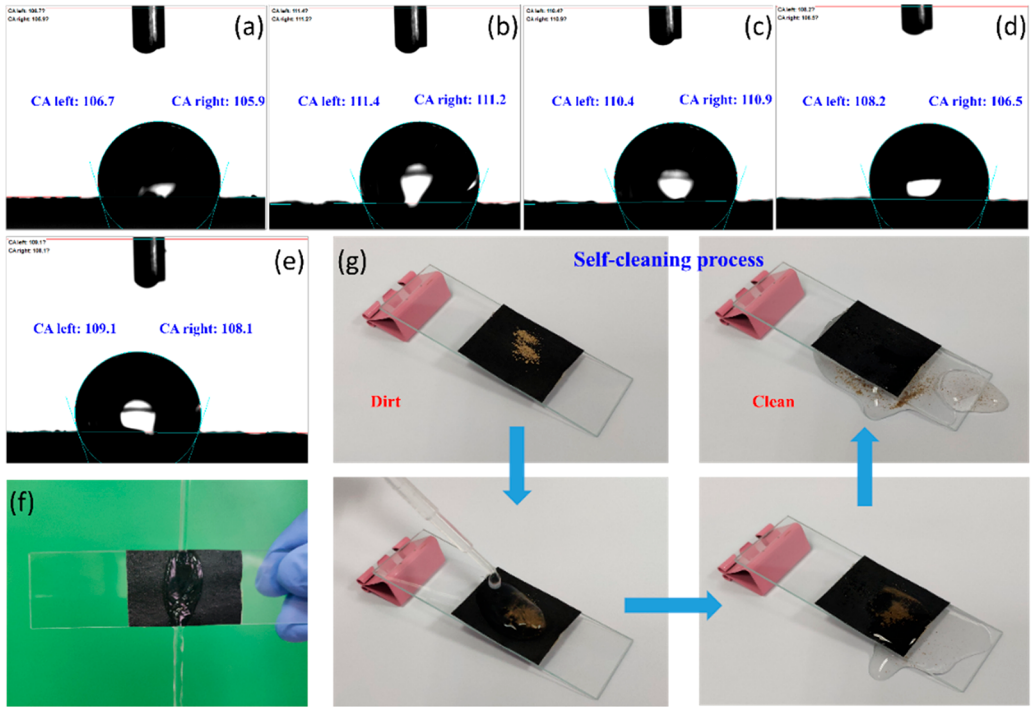

Figure 5. Water contact angles of PVDF-0.2Ag-2.0CNT/NWF (a), PVDF-0.6Ag-2.0CNT/NWF (b), PVDF-1.0Ag-2.0CNT/NWF (c), PVDF-1.4Ag-2.0CNT/NWF (d), and PVDF-1.9Ag-2.0CNT/NWF (e). The diagram of water flowing through the surface of the PVDF-based composite (f). Self-cleaning process of sandy soil on the PVDF-based composite (g).

composite. At first, the whole composite show elastic deformation. Then, after a plastic stage, they are finally fractured. As for the NWF, the Young's modulus is calculated as 26 MPa, and the maximum tensile strength is 7.9 MPa. Interestingly, compared with 2.0AgNWs/NWF (21 and 8.2 MPa), 2.0MWCNTs/NWF has a higher Young's modulus (157 MPa) and maximum tensile strength (9.2 MPa), which demonstrates 2.0MWCNTs/NWF possesses superior mechanical properties and indicates the MWCNTs show better strengthening effect (Figure S9a). After impregnating Ag NWs and MWCNTs onto the NWF, the Young's modulus and maximum tensile strength of the 1.9Ag-2.0CNT/NWF reach to 213 and 9.6 MPa, both of which are larger than the NWF, Ag NWs/NWF and MWCNTs/NWF. Since the MWCNTs and Ag NWs have a large aspect ratio, they can be embedded in the interior of the NWF, which makes the original fiber network structure of the NWF be denser and thus improves mechanical properties of the NWF. For pure PVDF (Figure S9b), the Young's modulus and maximum tensile strength are 1.8 GPa and 44.12 MPa, respectively. Thus, by casting the PVDF solution onto the NWF, the Young's modulus and maximum tensile strength of the PVDF-1.9Ag-2.0CNT/NWF increase to 952 and 17.9 MPa. Obviously, this result is attributed to the strengthening effect of the PVDF polymer. The tensile tests manifest the outstanding mechanical strength of the as-prepared PVDF-based composite, which makes it difficult to be destroyed in practical applications.

3.2. Hydrophobic Self-Cleaning Performance of the PVDF-Based Composite. Moisture problem of the external environment often existed in practical applications, which may cause negative effects on properties of the electronic device. Therefore, it is necessary to study the surface hydrophobic property of the material. Figure 5 shows the surface wettability of the PVDF-based composite. The water contact angles (CA) measurement indicates that the CA of PVDF-0.2Ag-2.0CNT/NWF, PVDF-0.6Ag-2.0CNT/NWF, PVDF-1.0Ag-2.0CNT/NWF, PVDF-1.4Ag-2.0CNT/NWF, and PVDF-1.9Ag-2.0CNT/NWF is up to 106.3°, 111.3°, 110.7°, 107.4°, and 108.6°, respectively, which demonstrates the excellent surface hydrophobicity of the PVDF-based composite. Besides, the PVDF/NWF and PVDF-2.0CNT/NWF show similar hydrophobicity to PVDF-Ag-2.0CNT/NWF and the water contact angles are 108.1° and 115.0°(Figure S10). Here, the surface of the NWF is hydrophilic, so the hydrophobicity of the PVDF-based composite is mainly caused by the casting of the hydrophobic PVDF polymer. The water flow contacting test further proves the water repellency of the PVDF-based composite (Figure 5f). When the water flow touches the surface, it can freely roll away from the surface without wetting. Based on the excellent water repellency, the self-cleaning performance of PVDF-1.9Ag-2.0CNT/NWF was studied. As can be seen in Figure 5g, the pollutants (sandy soil) on the surface can quickly leave from the surface under the running water flows, making the surface change from dirty to clean. Therefore, the surface hydrophobicity enables the PVDF-based composite to be immune to the outside rain and endows the composite with self-cleaning ability.

3.3. Electromagnetic Interference (EMI) Shielding Performance of the PVDF-Based Composite. According to the literature,[9,48] the attenuation of a material to electromagnetic waves can be defined as the total EMI shielding effectiveness (SE_T), which includes three components: the SE of reflection (SE_R), absorption (SE_A), and multiple reflections (SE_M). Usually, the SE_M value can be neglected if the SE_T is above 15 dB. Therefore, the EMI SE can be expressed as

$$SE_T = SE_A + SE_R$$

DOI: 10.1021/acsami.9b16120
ACS Appl. Mater. Interfaces 2019, 11, 47340−47349

The value of SE_T, SE_A, and SE_R were determined on the basis of the S parameters measured by the vector network analyzer as follows:

$$R = 10^{(S_{11}/10)}, \quad T = 10^{(S_{21}/10)}, \quad A = 1 - R - T$$

$$SE_R = -10\log(1 - R), \quad SE_A = -10\log(T/(1 - R)),$$
$$SE_T = SE_R + SE_A = -10\log T$$

where R is reflection coefficient, T is transmission coefficient, and A is absorption coefficient.

To verify the EMI shielding performance of the as-prepared PVDF-based composite, the SE_T, SE_A, and SE_R values were tested under 8.2−12.4 GHz (X-Band) frequency ranges. As shown in Figure 6a, the pure PVDF does not exhibit

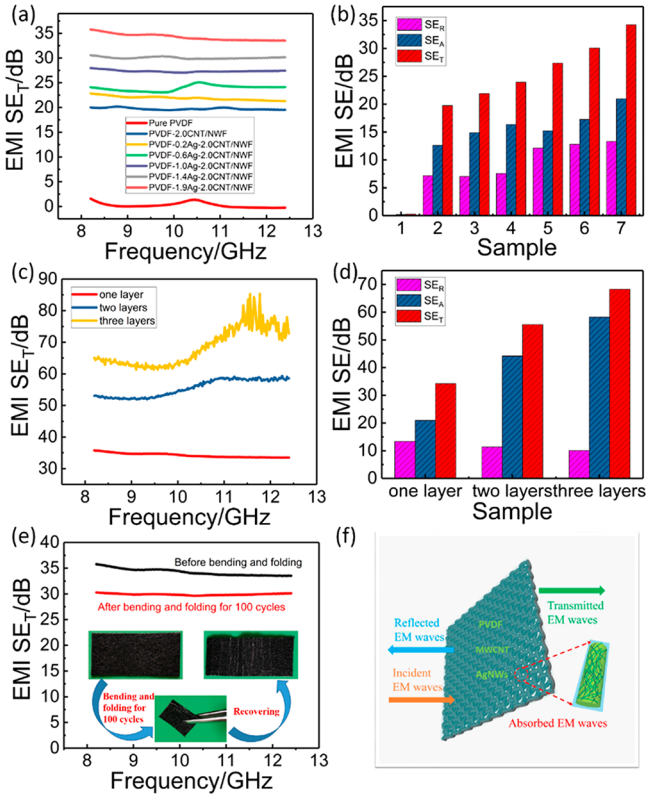

Figure 6. EMI SE_T (a) and SE_T, SE_A, and SE_R values of the pure PVDF, PVDF-2.0CNT/NWF, PVDF-0.2Ag-2.0CNT/NWF, PVDF-0.6Ag-2.0CNT/NWF, PVDF-1.0Ag-2.0CNT/NWF, PVDF-1.4Ag-2.0CNT/NWF, and PVDF-1.9Ag-2.0CNT/NWF (b). EMI SE_T (c) and SE_T, SE_A, and SE_R values of the PVDF-1.9Ag-2.0CNT/NWF with different layers (d). EMI SE_T variation of the PVDF-1.9Ag-2.0CNT/NWF before and after bending and folding for 100 cycles (e). The inset shows the bending and recovering state. Schematic EMI shielding mechanism of the PVDF-based composite (f).

electromagnetic shielding characteristic because of its insulation. After dipping MWCNTs and casting PVDF onto the NWF, the EMI SE_T value of PVDF-2.0CNT/NWF is 20 dB, which has met commercial requirements. Besides, the EMI SE_T value of the PVDF-CNT/NWF with 1.6 and 1.8 mg/cm^2 MWCNTs contents is also shown in Figure S11. The result reveals that the electromagnetic shielding performance increases with the increase of MWCNTs content. According to the EMI shielding mechanism (Figure 6f): (1) Materials absorb electromagnetic radiation by the interaction of electric and magnetic dipoles with the incident electromagnetic waves; thus the higher the dielectric constant, the higher the EMI SE_A value of the material. (2) Because of the interaction between free electrons and the electromagnetic wave, materials with high conductivity exhibit high EMI SE_R value. In general, high conductivity is an important factor in determining the EMI shielding performance. Therefore, the conductive MWCNTs greatly improve the EMI SE_T value. In order to enhance the EMI shielding performance, conductive Ag NWs were also added. It can be seen that with the increase of Ag NWs content, the EMI SE_T value also increases (Figure 6a). More Ag NWs form more effective conductive paths, thus leading to higher conductivity (Figure S12). When implementing 1.9 mg/cm^{2}Ag NWs and 2.0 mg/cm^2 MWCNT onto the PVDF/NWF, the maximum shielding value can be up to 34 dB. To further understand the hybrid shielding performance of Ag NWs and MWCNTs, the EMI data for PVDF-2.0Ag/NWF, PVDF-4.0Ag/NWF, and PVDF-4.0CNT/NWF has been provided in Figure S13. Figure S13a shows the EMI SE_T value of PVDF-2.0CNT/NWF and PVDF-2.0Ag/NWF, which indicates that PVDF-Ag/NWF has better EMI shielding performance than PVDF-CNT/NWF when the content of Ag NWs and MWCNTs is the same. Therefore, to assemble superior electromagnetic shielding material, Ag NWs are a kind of ideal conductive filler. However, considering that Ag NWs are expensive and easy to be oxidized, we chose conductive MWCNTs as another kind of filler. Furthermore, MWCNTs possess good mechanical strength and toughness. Figure S13b reveals the EMI SE_T value of PVDF-4.0CNT/NWF, PVDF-1.9Ag-2.0CNT/NWF, and PVDF-4.0Ag/NWF. Compared with PVDF-4.0Ag/NWF, the hybrid PVDF-1.9Ag-2.0CNT/NWF shows worse electromagnetic shielding performance, but it is better than PVDF-4.0CNT/NWF. Although the hybrid formation has slightly worse EMI shielding performance results than PVDF-Ag/NWF at similar loading, considering the electromagnetic shielding performance and mechanical properties, we did not choose single Ag NWs as the only conductive filler but chose to combine it with MWCNTs.

On the other hand, compared with PVDF-Ag-2.0CNT/NWF, the electromagnetic interference (EMI) shielding performance of PVDF-Ag/NWF (without MWCNTs) was also explored in Figure S14. It can be seen that the EMI shielding values of PVDF-Ag/NWF increase from 6 to 24 dB with the Ag NWs density increasing from 0.2 to 1.9 mg/cm^2(Figure S14a). After adding MWCNTs, the EMI shielding values of PVDF-Ag-2.0CNT/NWF are all higher than PVDF-Ag/NWF at the same Ag NWs density (Figure S14c). Similarly, when Ag NWs are added, the EMI shielding values of PVDF-Ag-2.0CNT/NWF are all higher than PVDF-2.0CNT/NWF at the same Ag NWs density (Figure S14d). For example, the EMI shielding values of PVDF-2.0CNT/NWF and PVDF-1.0Ag/NWF are 20 and 15 dB, respectively, and after combining MWCNTs and Ag NWs, the EMI shielding value of PVDF-1.0Ag-2.0CNT/NWF reaches to 27 dB, which is higher than PVDF-2.0CNT/NWF (20 dB) and PVDF-1.0Ag/NWF (15 dB). Therefore, the performance of electromagnetic shielding produced by the combination of Ag NWs and MWCNTs is larger than that of a single Ag NWs or MWCNTs, which clarifies the synergistic effect of Ag NWs and MWCNTs. Finally, to explore the primary EMI shielding mechanism of the as-prepared PVDF-based composite, the values of SE_T, SE_R, and SE_A were exhibited in Figure 6b. For all samples, SE_A was always higher than SE_R, indicating the EMI

DOI: 10.1021/acsami.9b16120
ACS Appl. Mater. Interfaces 2019, 11, 47340−47349

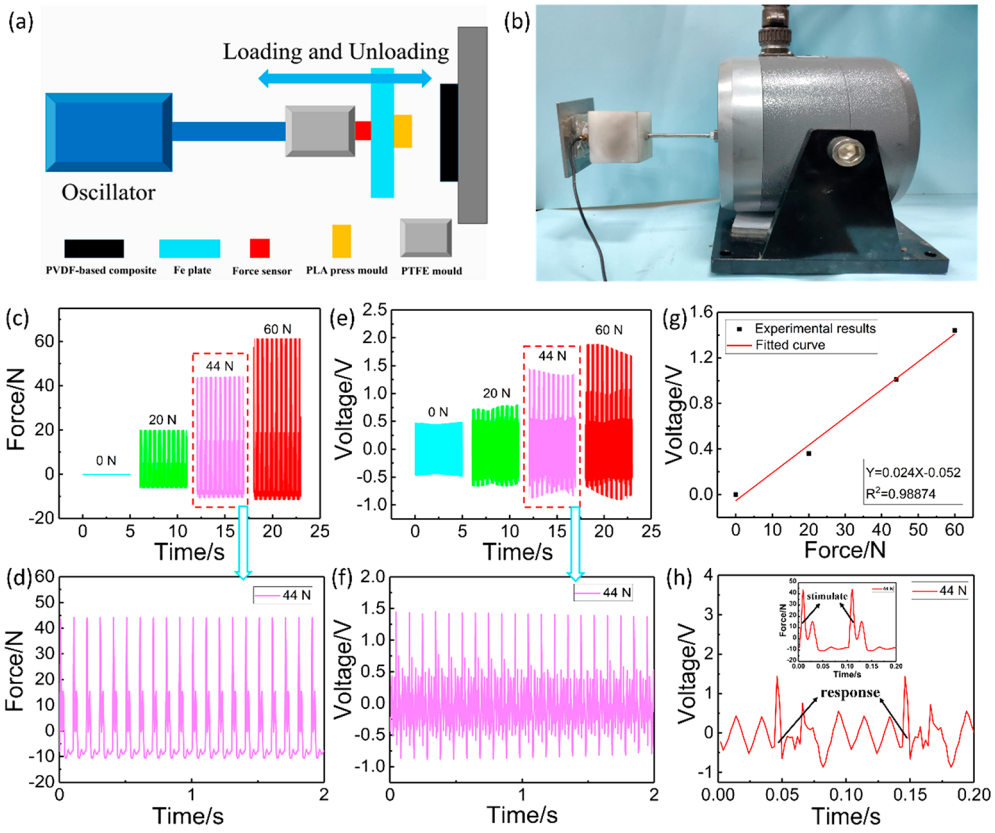

Figure 7. Schematic diagram of the loading and unloading excitation for sensing force produced by an oscillator (a) and the digital picture of the oscillator (b). The different forces loaded by the oscillator (c) and the corresponding enlarged view of the 44 N loading force (d). The piezoelectric voltage of the PVDF-1.9Ag-2.0CNT/NWF under different loading forces at the frequency of 10 Hz (e) and the enlarged view of the voltage generated by 44 N loading force (f). The linear fitting curve (g) and the response time (h) of the loading force and piezoelectric voltage.

shielding mechanism is mainly by the absorption of electromagnetic radiation.

For further improving the shielding performance, the EMI SE_T of PVDF-1.9Ag-2.0CNT/NWF with different layers was tested. Through measurement, the thickness of each layer was about 391, 393, and 390 μm, respectively, which showed a slight difference. Thus, the thicknesses of 1, 2, and 3 layers were approximately 391, 784, and 1174 μm. As expected, the EMI SE_T increases with the number of layer. The EMI SE_T reaches to 34, 55, and 70 dB under 1, 2, and 3 layers, respectively (Figure 6c). Regardless of the number of layers, SE_A was also higher than SE_R, which supports the absorption-dominant shielding mechanism of the PVDF-based composite (Figure 6d). Besides, it can be found that the sample layer causes less effect on the SE_R, which is explained by the fact that SE_R is mainly related to the impedance of the material surface and is independent of the number of material layers. Figure 6e shows the EMI SE_T variation of the PVDF-1.9Ag-2.0CNT/NWF before and after repeated bending and folding. Since the surface casting of the PVDF polymer endows the material with ideal mechanical strength and flexibility, the PVDF-1.9Ag-2.0CNT/NWF can maintain 85% EMI SE_T after 100 cycles, which guarantees the excellent EMI shielding stability and durability. To further confirm the reliability of the developed composite, a cyclic bending test and a water impacting test were also carried out (Figure S15). Therefore, the as-prepared PVDF-based composite possesses outstanding EMI shielding performance and can protect the human body from electromagnetic radiation.

3.4. Force-Sensing Performance of the PVDF-Based Sensor. According to the above EMI shielding tests, the PVDF-1.9Ag-2.0CNT/NWF composite show the optimal shielding performance. Thus, the PVDF-1.9Ag-2.0CNT/NWF composite is employed for the piezoelectric sensing test. Figure 7 displays the force-sensing performance of the PVDF-1.9Ag-2.0CNT/NWF composite with a size of 3 × 6 cm^2. The test system mainly consists of the sample, oscillator, and force sensor (Figure 7a,b). The sample was fixed to a flat plate and then stimulated by different external forces loaded by the oscillator. The different loading forces were recorded by a force sensor installed near the oscillator (Figure 7c,d), and the piezoelectric signal was recorded by a digital multimeter (DMM6001) (Figure 7e,f). Here, it is necessary to point out that when the sample is not subjected to external forces (0 N), a background electric signal of about 0.5 V can be observed, mainly because of the imperfect conditions under the double-electrode test method. It can be seen that the PVDF-based composite exhibits superior electric performance. When the force varies from 0 to 20, 44, and 60 N, the piezoelectric voltage of the PVDF-1.9Ag-2.0CNT/NWF increases proportionally from 0 to 0.4, 1.0, and 1.5 V, respectively. Because of the limitation of the experimental condition, 60 N is the maximum external force that the oscillator can load. By fitting, the force and voltage show a good linear relationship, and the response sensitivity is calculated as 0.024 V/N, indicating the as-prepared PVDF-based composite can sense different loading forces (Figure 7g). Moreover, this force-sensing performance exhibits a real-time property, and the response time is

DOI: 10.1021/acsami.9b16120
ACS Appl. Mater. Interfaces 2019, 11, 47340−47349

measured as 35 ms (Figure 7h). Based on the XRD and FTIR results, the as-fabricated PVDF-based composite contains an obvious γ-piezoelectric phase, which provides favorable support for showing the positive piezoelectric effect. The larger loading forces will induce the larger deformation of the PVDF-based composite, thus leading to the higher piezoelectric voltages. In addition, the loading force and piezoelectric voltage signals also show excellent stability under 44 N (Figure 7d,f). Besides, the cyclic stability of PVDF-1.9Ag-2.0CNT/NWF device under different forces (20, 44, and 60) was also magnified and displayed in Figure S16, which indicated the product possessed high reliability on the force-sensing performance. To this end, the developed PVDF-based composite exhibits superior sensing performance, which is expected to be applied in monitoring human body movements.

3.5. Human Body Monitoring Performance of the PVDF-Based Sensor. In order to examine the feasibility and practicability of the as-fabricated PVDF-based composite as a self-powered wearable sensor toward human body motions, it was attached to different positions of human body, and the piezoelectric sensing performance was depicted in Figure 8.

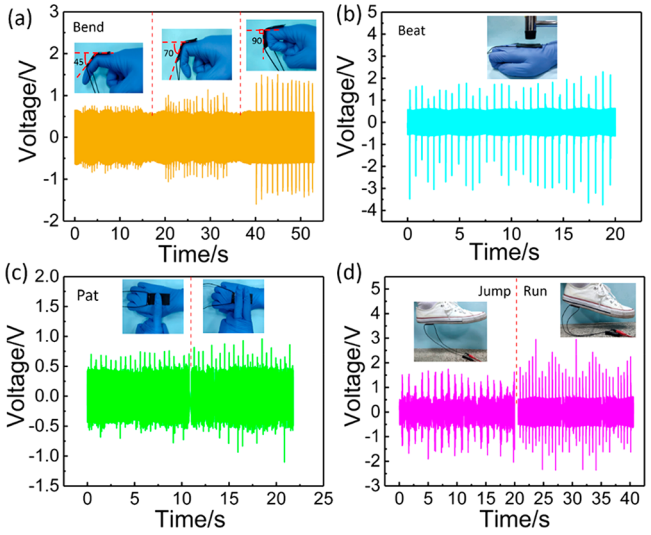

Figure 8. Photographs and the corresponding piezo-response with respect to output voltage signal of the PVDF-1.9Ag-2.0CNT/NWF sensor to monitor different human body movements: finger joint bending (a), beating (b), patting (c), and foot motions (d).

Interestingly, when the finger joint bends from 45° to 70° and 90°, the sensor can response the stimulus by changing voltage from 0.16 to 0.39 and 0.75 V. The larger bending angle leads to the higher voltage signal (Figure 8a). In Figure 8b,c, during the lightly patting process with different fingers, the PVDF-based sensor generates lower output voltage compared with that under hardly beating with a hammer, which shows that the piezoelectric sensing performance is related not only to the applied stress but also to the active contacting area. According to the mechanism of piezoelectricity, the piezoelectric properties of the PVDF-based composite primarily depend on the arrangement of different dipoles in the PVDF chains. In the absence of electric polarization, the arrangement of dipoles depends on the stress applied on the sensor. The larger stress and active piezoelectric area lead to the larger deformation of the crystal structure; thus, a higher output voltage will be obtained. Additionally, different motion states of foot (such as running and jumping) can also be clearly distinguished by fixing the sensor to the bottom of the shoe (Figure 8d).

Besides, it can be seen from Figure 8 that the noise signal is approximately 0.5 V. In this work, the double-electrode method was adopted to test the output voltage signal of PVDF-1.9Ag-2.0CNT/NWF device. The conductive copper tape as the upper and lower surface electrodes were connected with the digital multimeter via the wire. To prevent the charge leakage caused by contact with the outside, a layer of black insulation tape was affixed to the electrode. Because of the double-electrode method, the whole test system was inconvenient to always connect the wire to the ground in practical applications. On this occasion, the background noise of about 0.5 V was generated. Although the noise value of voltage in Figure 8 was a little big, the reported PVDF-based device showed distinguished output voltage signals on various occasions which could act as a self-powered force sensor to monitor different kinds of human movements. The signal-to-noise ratio (SNR) under different human motion occasions is calculated and shown in Table S1. Therefore, it can be concluded the as-prepared PVDF-based sensor exhibits broad prospects in the development of the human-based self-powered area, and it is significant in epidermal electronic system devices and medical applications of monitoring patient motions.

4. CONCLUSIONS

In this work, a multifunctional PVDF-based composite with effective electromagnetic interference (EMI) shielding and human body monitoring performance is constructed by integrating conductive Ag NWs and MWCNTs into a modified nonwoven fabrics (NWF) with piezoelectric PVDF matrix. The EMI shielding experiment shows that the maximum shielding value can reach up to 34 dB when implementing 1.9 mg/cm^{2}Ag NWs and 2.0 mg/cm^2 MWCNT onto the NWF, demonstrating wonderful protection ability of the human body with superior shielding performance. More importantly, the as-prepared PVDF-based composite can not only protect the human body from electromagnetic radiation but also monitor different movements of the human body, such as joint bending and foot movements, which is attributed to the piezoelectric sensing property of the PVDF composite. Additionally, the contact angle experiment indicates the PVDF-based composite possesses excellent hydrophobicity, which guarantees the self-cleaning performance and can be protected from natural rain and water. Finally, these wide-ranging performances vastly expand the potential applications of the as-fabricated PVDF-based composite, which adapts to the demand of multifunctional properties of the material in the new era.

■ ASSOCIATED CONTENT

Supporting Information

The Supporting Information is available free of charge at https://pubs.acs.org/doi/10.1021/acsami.9b16120.

The SEM and TEM images of MWCNTs; the SEM images, elemental mapping images and EDS spectrum of nonwoven fabrics (NWF), 1.9Ag NWs/NWF, 2.0CNT/NWF and 1.9Ag NWs-2.0CNT/NWF; the γ-phase content of pure PVDF, PVDF/NWF, PVDF-2.0CNT/NWF and PVDF-1.9Ag-2.0CNT/NWF composite; P-E hysteresis loops and strain-electric field curves of PVDF-1.9Ag-2.0CNT/NWF composite; the tensile stress−strain curves of 2.0CNT/NWF, 2.0Ag/NWF, NWF

DOI: 10.1021/acsami.9b16120
ACS Appl. Mater. Interfaces 2019, 11, 47340−47349

and pure PVDF; the water contact angles of PVDF/NWF and PVDF-2.0CNT/NWF; the electrical conductivity of NWF, 2.0CNT/NWF, Ag/NWF and Ag-2.0CNT/NWF; EMI SE_T value of PVDF-2.0CNT/NWF, PVDF-2.0Ag/NWF, PVDF-4.0CNT/NWF, PVDF-1.9Ag-2.0CNT/NWF, PVDF-4.0Ag/NWF, PVDF-Ag/NWF, PVDF-CNT/NWF and PVDF-Ag-2.0CNT/NWF, the EMI shielding performance comparison of PVDF-Ag/NWF and PVDF-Ag-2.0CNT/NWF, and of PVDF-2.0CNT/NWF and PVDF-Ag-2.0CNT/NWF; the EMI SE_T value of PVDF-1.9Ag-2.0CNT/NWF composite before and after water impact and bending test; The cyclic stability of PVDF-1.9Ag-2.0CNT/NWF device under different forces; The signal-to-noise ratio (SNR) under different human motion occasions in Figure 8 (PDF)

AUTHOR INFORMATION

Corresponding Authors

*E-mail for W.Q.J.: jiangwq@ustc.edu.cn. Tel: 86-551-63607605. Fax: 86-551-63600419

*E-mail for X.L.G.: gongxl@ustc.edu.cn.

*E-mail for S.H.X.: xuansh@ustc.edu.cn.

ORCID

Wanquan Jiang: 0000-0002-8044-1783

Shouhu Xuan: 0000-0002-8232-9736

Xinglong Gong: 0000-0001-6997-9526

Notes

The authors declare no competing financial interest.

ACKNOWLEDGMENTS

Financial supports from the National Natural Science Foundation of China (Grant Nos. 11822209, 11572309, 11572310) and the Strategic Priority Research Program of the Chinese Academy of Sciences (Grant No. XDB22040502) are gratefully acknowledged. This work is also supported by the Collaborative Innovation Center of Suzhou Nano Science and Technology.

ABBREVIATIONS

PVDF, polyvinylidene fluoride
Ag NWs, silver nanowire
MWCNTs, multiwalled carbon nanotubes
NWF, nonwoven fabrics
EMI shielding, electromagnetic interference shielding
NMP, *N*-methyl pyrrolidone
SEM, Scanning Electron Microscopy
TEM, Transmission Electron Microscopy
XRD, X-ray diffraction
FTIR, the Fourier Transform Infrared Spectroscopy
P-E loop, polarization-electric field loop
MTS, the Material Test System
CA, Contact Angles
SE, shielding effectiveness
SE_T, the total SE
SE_R, the SE of reflection
SE_A, the SE of absorption
SE_M, the SE of multiple reflections

REFERENCES

(1) Jia, L. C.; Zhang, G.; Xu, L.; Sun, W. J.; Zhong, G. J.; Lei, J.; Yan, D. X.; Li, Z. M. Robustly Superhydrophobic Conductive Textile for Efficient Electromagnetic Interference Shielding. *ACS Appl. Mater. Interfaces* **2019**, *11*, 1680−1688.

(2) Song, Q.; Ye, F.; Yin, X.; Li, W.; Li, H.; Liu, Y.; Li, K.; Xie, K.; Li, X.; Fu, Q.; Cheng, L.; Zhang, L.; Wei, B. Carbon Nanotube-Multilayered Graphene Edge Plane Core-Shell Hybrid Foams for Ultrahigh-Performance Electromagnetic-Interference Shielding. *Adv. Mater.* **2017**, *29*, 1701583.

(3) Huang, H.-D.; Liu, C.-Y.; Zhou, D.; Jiang, X.; Zhong, G.-J.; Yan, D.-X.; Li, Z.-M. Cellulose Composite Aerogel for Highly Efficient Electromagnetic Interference Shielding. *J. Mater. Chem. A* **2015**, *3*, 4983−4991.

(4) Liu, Y.; Lu, M.; Wu, K.; Yao, S.; Du, X.; Chen, G.; Zhang, Q.; Liang, L.; Lu, M. Anisotropic Thermal Conductivity and Electromagnetic Interference Shielding of Epoxy Nanocomposites Based on Magnetic Driving Reduced Graphene Oxide@Fe_3O_4. *Compos. Sci. Technol.* **2019**, *174*, 1−10.

(5) Wang, Y. N.; Cheng, X. D.; Song, W. L.; Ma, C. J.; Bian, X. M.; Chen, M. J. Hydro-Sensitive Sandwich Structures for Self-Tunable Smart Electromagnetic Shielding. *Chem. Eng. J.* **2018**, *344*, 342−352.

(6) Zhao, S.; Zhang, H. B.; Luo, J. Q.; Wang, Q. W.; Xu, B.; Hong, S.; Yu, Z. Z. Highly Electrically Conductive Three-Dimensional Ti_3C_2Tx MXene/Reduced Graphene Oxide Hybrid Aerogels with Excellent Electromagnetic Interference Shielding Performances. *ACS Nano* **2018**, *12*, 11193−11202.

(7) Zhang, Y.; Tian, W.; Liu, L.; Cheng, W.; Wang, W.; Liew, K. M.; Wang, B.; Hu, Y. Eco-Friendly Flame Retardant and Electromagnetic Interference Shielding Cotton Fabrics with Multi-Layered Coatings. *Chem. Eng. J.* **2019**, *372*, 1077−1090.

(8) Zhou, E.; Xi, J.; Guo, Y.; Liu, Y.; Xu, Z.; Peng, L.; Gao, W.; Ying, J.; Chen, Z.; Gao, C. Synergistic Effect of Graphene and Carbon Nanotube for High-Performance Electromagnetic Interference Shielding Films. *Carbon* **2018**, *133*, 316−322.

(9) Vinod, K. R.; Saravanan, P.; Suresh Kumar, T. R.; Radha, R.; Balasubramanniam, M.; Balakumar, S. Enhanced Shielding Effectiveness in Nanohybrids of Graphene Derivatives with Fe_3O_4 and Epsilon-Fe_3N in the X-Band Microwave Region. *Nanoscale* **2018**, *10*, 12018−12034.

(10) Li, X.; Yin, X.; Liang, S.; Li, M.; Cheng, L.; Zhang, L. 2D Carbide MXene Ti_2CT_X as ANovel High-Performance Electromagnetic Interference Shielding Material. *Carbon* **2019**, *146*, 210−217.

(11) Shahzad, F.; Alhabeb, M.; Hatter, C. B.; Anasori, B.; Man Hong, S.; Koo, C. M.; Gogotsi, Y. Electromagnetic Interference Shielding with 2D Transition Metal Carbides (MXenes). *Science* **2016**, *353*, 1137−1140.

(12) Wan, Y. J.; Zhu, P. L.; Yu, S. H.; Sun, R.; Wong, C. P.; Liao, W. H. Anticorrosive, Ultralight, and Flexible Carbon-Wrapped Metallic Nanowire Hybrid Sponges for Highly Efficient Electromagnetic Interference Shielding. *Small* **2018**, *14*, 1800534.

(13) Wu, S.; Zou, M.; Li, Z.; Chen, D.; Zhang, H.; Yuan, Y.; Pei, Y.; Cao, A. Robust and Stable Cu Nanowire@Graphene Core-Shell Aerogels for Ultraeffective Electromagnetic Interference Shielding. *Small* **2018**, *14*, 1800634.

(14) Kumaran, R.; Kumar, S. D.; Balasubramanian, N.; Alagar, M.; Subramanian, V.; Dinakaran, K. Enhanced Electromagnetic Interference Shielding in a Au−MWCNT Composite Nanostructure Dispersed PVDF Thin Films. *J. Phys. Chem. C* **2016**, *120*, 13771−13778.

(15) Li, Y.; Li, C.; Zhao, S.; Cui, J.; Zhang, G.; Gao, A.; Yan, Y. Facile Fabrication of Highly Conductive and Robust Three-Dimensional Graphene/Silver Nanowires Bicontinuous Skeletons for Electromagnetic Interference Shielding Silicone Rubber Nanocomposites. *Composites, Part A* **2019**, *119*, 101−110.

(16) Wang, Y.; Gu, F. Q.; Ni, L. J.; Liang, K.; Marcus, K.; Liu, S. L.; Yang, F.; Chen, J. J.; Feng, Z. S. Easily Fabricated and Lightweight PPy/PDA/AgNW Composites for Excellent Electromagnetic Interference Shielding. *Nanoscale* **2017**, *9*, 18318−18325.

(17) Zeng, Z.; Chen, M.; Jin, H.; Li, W.; Xue, X.; Zhou, L.; Pei, Y.; Zhang, H.; Zhang, Z. Thin and Flexible Multi-Walled Carbon

DOI: 10.1021/acsami.9b16120
ACS Appl. Mater. Interfaces 2019, 11, 47340−47349

Nanotube/Waterborne Polyurethane Composites with High-Performance Electromagnetic Interference Shielding. *Carbon* **2016**, *96*, 768−777.
(18) Wang, G.; Wang, L.; Mark, L. H.; Shaayegan, V.; Wang, G.; Li, H.; Zhao, G.; Park, C. B. Ultralow-Threshold and Lightweight Biodegradable Porous PLA/MWCNT with Segregated Conductive Networks for High-Performance Thermal Insulation and Electromagnetic Interference Shielding Applications. *ACS Appl. Mater. Interfaces* **2018**, *10*, 1195−1203.
(19) Wang, S.; Ding, L.; Fan, X.; Jiang, W.; Gong, X. A Liquid Metal-Based Triboelectric Nanogenerator as Stretchable Electronics for Safeguarding and Self-Powered Mechanosensing. *Nano Energy* **2018**, *53*, 863−870.
(20) Xu, S.; Vogt, D. M.; Hsu, W.-H.; Osborne, J.; Walsh, T.; Foster, J. R.; Sullivan, S. K.; Smith, V. C.; Rousing, A. W.; Goldfield, E. C.; Wood, R. J. Biocompatible Soft Fluidic Strain and Force Sensors for Wearable Devices. *Adv. Funct. Mater.* **2019**, *29*, 1807058.
(21) Wang, Y.; Wang, Y.; Yang, Y. Graphene-Polymer Nanocomposite-Based Redox-Induced Electricity for Flexible Self-Powered Strain Sensors. *Adv. Energy Mater.* **2018**, *8*, 1800961.
(22) You, M.-H.; Wang, X.-X.; Yan, X.; Zhang, J.; Song, W.-Z.; Yu, M.; Fan, Z.-Y.; Ramakrishna, S.; Long, Y.-Z. A Self-Powered Flexible Hybrid Piezoelectric−Pyroelectric Nanogenerator Based on Non-Woven Nanofiber Membranes. *J. Mater. Chem. A* **2018**, *6*, 3500−3509.
(23) Ding, L.; Xuan, S.; Pei, L.; Wang, S.; Hu, T.; Zhang, S.; Gong, X. Stress and Magnetic Field Bimode Detection Sensors Based on Flexible CI/CNTs-PDMS Sponges. *ACS Appl. Mater. Interfaces* **2018**, *10*, 30774−30784.
(24) Pang, Y.; Zhang, K.; Yang, Z.; Jiang, S.; Ju, Z.; Li, Y.; Wang, X.; Wang, D.; Jian, M.; Zhang, Y.; Liang, R.; Tian, H.; Yang, Y.; Ren, T. L. Epidermis Microstructure Inspired Graphene Pressure Sensor with Random Distributed Spinosum for High Sensitivity and Large Linearity. *ACS Nano* **2018**, *12*, 2346−2354.
(25) Li, T.; Luo, H.; Qin, L.; Wang, X.; Xiong, Z.; Ding, H.; Gu, Y.; Liu, Z.; Zhang, T. Flexible Capacitive Tactile Sensor Based on Micropatterned Dielectric Layer. *Small* **2016**, *12*, 5042−5048.
(26) Lee, J.; Kwon, H.; Seo, J.; Shin, S.; Koo, J. H.; Pang, C.; Son, S.; Kim, J. H.; Jang, Y. H.; Kim, D. E.; Lee, T. Conductive Fiber-Based Ultrasensitive Textile Pressure Sensor for Wearable Electronics. *Adv. Mater.* **2015**, *27*, 2433−2439.
(27) Park, D. Y.; Joe, D. J.; Kim, D. H.; Park, H.; Han, J. H.; Jeong, C. K.; Park, H.; Park, J. G.; Joung, B.; Lee, K. J. Self-Powered Real-Time Arterial Pulse Monitoring Using Ultrathin Epidermal Piezoelectric Sensors. *Adv. Mater.* **2017**, *29*, 1702308.
(28) Zhong, Q.; Zhong, J.; Cheng, X.; Yao, X.; Wang, B.; Li, W.; Wu, N.; Liu, K.; Hu, B.; Zhou, J. Paper-Based Active Tactile Sensor Array. *Adv. Mater.* **2015**, *27*, 7130−7136.
(29) Zhang, B.; Zhang, L.; Deng, W.; Jin, L.; Chun, F.; Pan, H.; Gu, B.; Zhang, H.; Lv, Z.; Yang, W.; Wang, Z. L. Self-Powered Acceleration Sensor Based on Liquid Metal Triboelectric Nanogenerator for Vibration Monitoring. *ACS Nano* **2017**, *11*, 7440−7446.
(30) Jin, L.; Deng, W.; Su, Y.; Xu, Z.; Meng, H.; Wang, B.; Zhang, H.; Zhang, B.; Zhang, L.; Xiao, X.; Zhu, M.; Yang, W. Self-Powered Wireless Smart Sensor Based on Maglev Porous Nanogenerator for Train Monitoring System. *Nano Energy* **2017**, *38*, 185−192.
(31) Zhang, C.; Fan, Y.; Li, H.; Li, Y.; Zhang, L.; Cao, S.; Kuang, S.; Zhao, Y.; Chen, A.; Zhu, G.; Wang, Z. L. Fully Rollable Lead-Free Poly(vinylidene fluoride)-Niobate-Based Nanogenerator with Ultra-Flexible Nano-Network Electrodes. *ACS Nano* **2018**, *12*, 4803−4811.
(32) Mokhtari, F.; Foroughi, J.; Zheng, T.; Cheng, Z.; Spinks, G. M. Triaxial Braided Piezo Fiber Energy Harvesters for Self-Powered Wearable Technologies. *J. Mater. Chem. A* **2019**, *7*, 8245−8257.
(33) Karan, S. K.; Maiti, S.; Agrawal, A. K.; Das, A. K.; Maitra, A.; Paria, S.; Bera, A.; Bera, R.; Halder, L.; Mishra, A. K.; Kim, J. K.; Khatua, B. B. Designing High Energy Conversion Efficient Bio-Inspired Vitamin Assisted Single-Structured Based Self-Powered Piezoelectric/Wind/Acoustic Multi-Energy Harvester with Remarkable Power Density. *Nano Energy* **2019**, *59*, 169−183.
(34) Guo, R.; Zhang, H.; Cao, S.; Cui, X.; Yan, Z.; Sang, S. A Self-Powered Stretchable Sensor Fabricated by Serpentine PVDF Film for Multiple Dynamic Monitoring. *Mater. Des.* **2019**, *182*, 108025.
(35) Maity, K.; Mandal, D. All-Organic High-Performance Piezoelectric Nanogenerator with Multilayer Assembled Electrospun Nanofiber Mats for Self-Powered Multifunctional Sensors. *ACS Appl. Mater. Interfaces* **2018**, *10*, 18257−18269.
(36) Maity, K.; Garain, S.; Henkel, K.; Schmeisser, D.; Mandal, D. Natural Sugar-Assisted, Chemically Reinforced, Highly Durable Piezoorganic Nanogenerator with Superior Power Density for Self-Powered Wearable Electronics. *ACS Appl. Mater. Interfaces* **2018**, *10*, 44018−44032.
(37) Li, H.; Zhang, Y.; Dai, H.; Tong, W.; Zhou, Y.; Zhao, J.; An, Q. A Self-Powered Porous ZnS/PVDF-HFP Mechanoluminescent Composite Film that Converts Human Movement into Eye-Readable Light. *Nanoscale* **2018**, *10*, 5489−5495.
(38) Jin, L.; Ma, S.; Deng, W.; Yan, C.; Yang, T.; Chu, X.; Tian, G.; Xiong, D.; Lu, J.; Yang, W. Polarization-Free High-Crystallization β-PVDF Piezoelectric Nanogenerator toward Self-Powered 3D Acceleration Sensor. *Nano Energy* **2018**, *50*, 632−638.
(39) Zhang, Q.; Liang, Q.; Zhang, Z.; Kang, Z.; Liao, Q.; Ding, Y.; Ma, M.; Gao, F.; Zhao, X.; Zhang, Y. Electromagnetic Shielding Hybrid Nanogenerator for Health Monitoring and Protection. *Adv. Funct. Mater.* **2018**, *28*, 1703801.
(40) Pu, J. H.; Zha, X. J.; Tang, L. S.; Bai, L.; Bao, R. Y.; Liu, Z. Y.; Yang, M. B.; Yang, W. Human Skin-Inspired Electronic Sensor Skin with Electromagnetic Interference Shielding for the Sensation and Protection of Wearable Electronics. *ACS Appl. Mater. Interfaces* **2018**, *10*, 40880−40889.
(41) Yang, C.; Gu, H.; Lin, W.; Yuen, M. M.; Wong, C. P.; Xiong, M.; Gao, B. Silver Nanowires: From Scalable Synthesis to Recyclable Foldable Electronics. *Adv. Mater.* **2011**, *23*, 3052−3056.
(42) Ince-Gunduz, B. S.; Alpern, R.; Amare, D.; Crawford, J.; Dolan, B.; Jones, S.; Kobylarz, R.; Reveley, M.; Cebe, P. Impact of Nanosilicates on Poly(vinylidene fluoride) Crystal Polymorphism: Part 1. Melt-Crystallization at High Supercooling. *Polymer* **2010**, *51*, 1485−1493.
(43) Barrau, S.; Ferri, A.; Da Costa, A.; Defebvin, J.; Leroy, S.; Desfeux, R.; Lefebvre, J. M. Nanoscale Investigations of alpha- and gamma-Crystal Phases in PVDF-Based Nanocomposites. *ACS Appl. Mater. Interfaces* **2018**, *10*, 13092−13099.
(44) Lopes, A. C.; Caparros, C.; Gómez Ribelles, J. L.; Neves, I. C.; Lanceros-Mendez, S. Electrical and Thermal Behavior of γ-Phase Poly(vinylidene fluoride)/NaY Zeolite Composites. *Microporous Mesoporous Mater.* **2012**, *161*, 98−105.
(45) Li, Y.; Xu, J. Z.; Zhu, L.; Zhong, G. J.; Li, Z. M. Role of Ion-Dipole Interactions in Nucleation of gamma Poly(vinylidene fluoride) in the Presence of Graphene Oxide during Melt Crystallization. *J. Phys. Chem. B* **2012**, *116*, 14951−14960.
(46) Lopes, A. C.; Costa, C. M.; Tavares, C. J.; Neves, I. C.; Lanceros-Mendez, S. Nucleation of the Electroactive γ Phase and Enhancement of the Optical Transparency in Low Filler Content Poly(vinylidene)/Clay Nanocomposites. *J. Phys. Chem. C* **2011**, *115*, 18076−18082.
(47) Martins, P.; Lopes, A. C.; Lanceros-Mendez, S. Electroactive Phases of Poly(vinylidene fluoride): Determination, Processing and Applications. *Prog. Polym. Sci.* **2014**, *39*, 683−706.
(48) Sun, Y.; Luo, S.; Sun, H.; Zeng, W.; Ling, C.; Chen, D.; Chan, V.; Liao, K. Engineering Closed-Cell Structure in Lightweight and Flexible Carbon Foam Composite for High-Efficient Electromagnetic Interference Shielding. *Carbon* **2018**, *136*, 299−308.

DOI: 10.1021/acsami.9b16120
ACS Appl. Mater. Interfaces 2019, 11, 47340−47349